PROCEEDINGS OF SCIENCE

Calibrating the Surface Scintillator Detector of AugerPrime

Paul Filip[a,b,*] **for the Pierre Auger Collaboration**[c]

[a] *Institute for Astroparticle Physics, Karlsruhe Institute for Technology*
Hermann-von-Helmholtz Platz 1, 76344 Eggenstein-Leopoldshafen, Germany

[b] *Instituto de Tecnologias en Deteccion y Astroparticulas, Universidad Nacional de General San Martín*
Av. Gral. Paz 1499, B1650 Buenos Aires, Argentina

[c] *Pierre Auger Observatory*
Av. San Martín Norte 304, Malargüe, Mendoza, Argentina
Full author list: https://www.auger.org/archive/authors_2024_11.html

E-mail: spokespersons@auger.org

We present the methods used to calibrate the Surface Scintillator Detector of the Pierre Auger Observatory. We describe how to obtain an accurate calibration of the scintillator by examining peak and charge distributions of atmospheric muons. This is done whenever an extensive air shower event measured by the Surface Detector is reconstructed. We also describe the work towards an algorithm that uses a rate-based approach to calibrate the Surface Scintillator Detectors independently.

7th International Symposium on Ultra High Energy Cosmic Rays (UHECR) 2024
17–21 November 2024
Malargüe, Argentina

*Speaker

 ISSN 1824-8039 . Published by SISSA Medialab.

PoS(UHECR2024)085

1. Introduction

The Pierre Auger Observatory is an experiment designed to detect particles of extraterrestrial origin and study the sources that give them enormous energies. Its detectors cover an area of $3000\,\mathrm{km}^2$ and offer a unique view into the physical processes that occur at energies that are unattainable by particle accelerators on Earth. It uses a hybrid approach to detect Extensive Air Showers (EASs) developing in the atmosphere via the Fluorescence Detector (FD) and on the ground with the Surface Detector (SD).

The latter is a collection of more than 1600 autonomously operating stations, with a duty cycle of close to 100%. Each station consists of a cylindrical tank filled with water, three photomultiplier tubes (PMTs), readout, processing, and communication electronics. The water tank and mounted PMTs are commonly referred to as Water Cherenkov Detectors (WCDs). Several trigger algorithms scan the data measured by the WCD for the detection of an EAS.

The trigger criteria on the Local Station (LS) must be carefully set, as the uplink bandwidth for communication between an LS and the Central Data Acquisition System (CDAS) is limited. Trigger thresholds that are too permissive make the SD sensitive to noise. This results in a high trigger rate and could bottleneck the exchange of information between the CDAS and LS. To ensure constant LS trigger rates, the thresholds in the Surface Detector of the observatory are defined in terms of physical properties of particles. These properties must be measured continuously by calibration algorithms. Moreover, this calibration defines a common ground between measurements and simulations and ensures that data can be properly interpreted.

In recent years, the Pierre Auger Observatory underwent a major upgrade, named *AugerPrime*. This upgrade enhances Auger's sensitivity to the mass of the primary particle on an event-by-event basis by, among other things, adding information from a radio antenna and a scintillator detector on top of each station. The same considerations apply for both new detection channels: The measured data must be calibrated and given a physical meaning.

In this work, we present the methods used to calibrate the surface scintillator detector of the Pierre Auger Observatory. After a brief review of the detector hardware and readout in section 2, we explain the calibration approach in section 3. Section 4 details the calibration algorithm used during the reconstruction of EAS events. In section 5 we outline the work towards an algorithm that can calibrate the surface scintillator detector in every SD station independently.

2. Surface Scintillator Detector

The Surface Scintillator Detector (SSD) is a flat rectangular polystyrene scintillator with an active area of $3.84\,\mathrm{m}^2$ mounted on top of the WCD as seen in fig. 1a. The active detector volume is divided into two wings, which in turn are segmented into bars of 50 mm by 1600 mm by 10 mm ($\mathrm{W} \times \mathrm{L} \times \mathrm{H}$). Each bar houses two horizontal holes through which wavelength-shifting (WLS) fibers are guided [3]. The display of the detector setup is shown in fig. 1b.

A Hamamatsu R9420 PMT is placed between both wings and coupled to the ends of the WSL fibers via optical cement. The voltage at the anode of the PMT is digitized via a 12-bit FADC that has a sampling rate of 120 MHz. This corresponds to a binning of $8.\bar{3}$ ns. More details on the read-out procedure can be found in [6].

(a) **(b)**

Figure 1: **(a)** A rendering of an SD station with *AugerPrime* components. The SSD enclosure box (blueish tinted rectangle) is mounted on top of the (beige) WCD. **(b)** View of one wing of scintillator bars in an open enclosure box. The (green) WSL fibers guide light to a PMT visible in the bottom left. From [4].

The scale of values provided by the FADCs is difficult to interpret without exact knowledge of the electronic gain of the signal readout chain. For this reason, we define two units related to the characteristic energy deposit of minimally ionizing particles (MIPs) that give physical meaning to the signals measured in the scintillator detector.

1. $\boldsymbol{I}_{\mathrm{MIP}}$ gives the most probable pulse height recorded by the SSD when uniformly distributed MIPs pass vertically through the detector.

2. $\boldsymbol{Q}_{\mathrm{MIP}}$ defines the most probable sum of all signal, corresponding to the total energy deposited from uniformly distributed MIPs passing vertically through the SSD.

A visual explanation of the maximum pulse height and sum, also referred to as the MIP peak and charge, is given in fig. 2a. Both quantities are measured in analog-digital counts (ADCs) As the deposition of energy in the detectors is fundamentally stochastic for a single MIP, the most probable pulse height and sum are only well approximated over a sample of many MIPs.

3. Calibration method & event selection

The Pierre Auger Observatory uses muons originating from low-energy showers for the calibration of the WCD and SSD. Such muons are typically produced above the minimum of the Bethe-Bloch curve, and are thus minimally ionizing particles. Furthermore, their abundance makes them ideal candidates for the determination of I_{MIP} and Q_{MIP} with small statistical uncertainty.

3.1 Selection of muons

A simple-bin threshold trigger scans the data of the four different PMTs (3 WCD, 1 SSD), and searches for an excess of 30 ADC (70 ADC) above the estimated baseline for the WCD (SSD). The WCD threshold is chosen such that nearly all muons passing the WCD satisfy these trigger criteria, regardless of the electronic gain of the PMTs [5]. Once such a muon trigger is issued, the

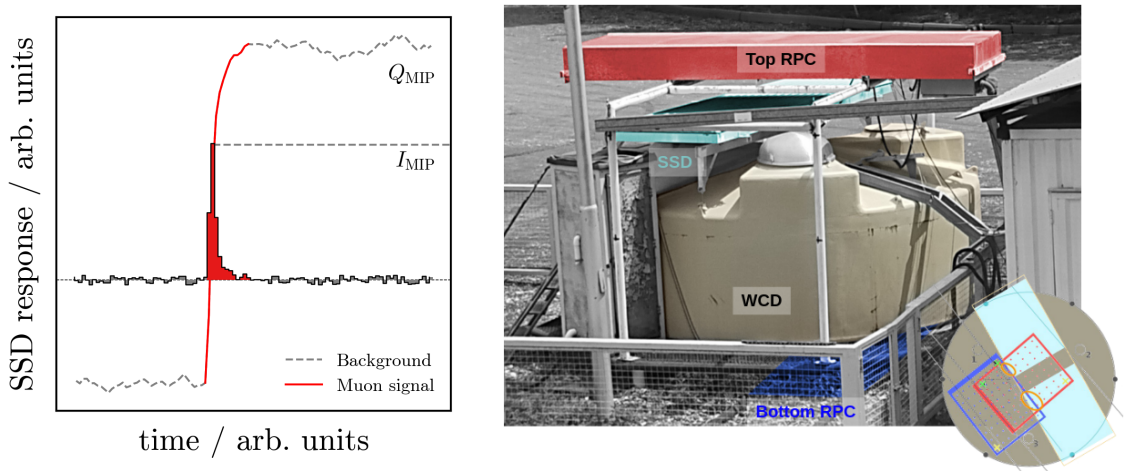

(a) **(b)**

Figure 2: **(a)** Example response recorded by the SSD PMT when a muon (red) hits the detector. I is defined as the pulse height recorded during this interaction. Q is the cumulative sum of individual pulse heights, as shown by the lineplot. For visualization purposes, the lineplot is offset downwards. **(b)** The experimental setup to determine the conversion factor between vertical and omnidirectional MIPs. An SD station (WCD and SSD) is placed in a hodoscope consisting of an RPC on top (red) and on the bottom (blue). The inset on the bottom right offers a view of the schematic from the top.

information from all four PMTs is read over a window of 575 ns (19 bins before the trigger latch bin, and 39 bins afterwards) and stored for further processing (cf. section 4 and section 5).

3.2 Vertical vs. omnidirectional MIP

I_{MIP} and Q_{MIP} are defined as the characteristics of MIPs that pass through the full area of the detector *vertically*. Meanwhile, the SD stations are bombarded by particles from all directions. Since the track length in the SSD for inclined particles is longer than for vertical particles, this influences the mean energy deposit recorded in the detector.

The hardware available in a standard SD station does not allow for the selection of vertical particles. I_{MIP} and Q_{MIP} cannot be measured directly as a consequence. We address this by applying a constant scaling factor to the calculated peak and charge values.

The value of this scaling factor will be measured experimentally. An SD station with WCD and SSD is equipped with a hodoscope consisting of two resistive plate chambers (RPCs) above and below the detectors. The setup is shown in fig. 2b and is described in more detail in [7]. We select vertical events by only considering SSD data that have a corresponding trigger in the top and bottom RPCs. As expected, we find that the mean energy deposit for vertical events is lower due to a shorter track length in the detector. This is visualized in fig. 3b.

4. Histogram based calibration

Muon-like events are continuously collected on all SD stations (cf. section 3.1). From this collection of data, we pick those events where at least one of the WCD PMTs satisfies the muon

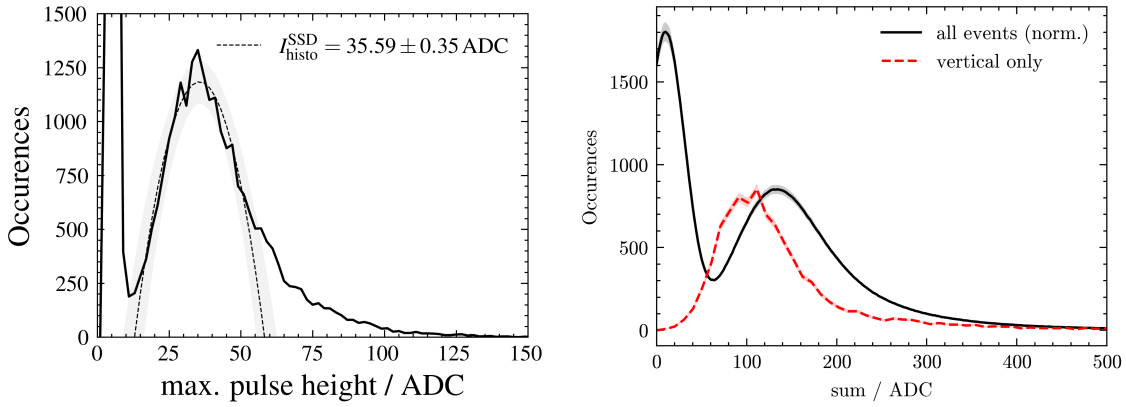

Figure 3: **(a)** Example distribution of max. pulse heights I in the scintillator detector of a local station, collected over 61 s. The local maxima around 40 ADC ties to the most probable energy deposit of a MIP. A parabola (dashed black line) is fitted to the structure to obtain the value of $I^{\mathrm{SSD}}_{\mathrm{histo}}$. **(b)** The distribution of the sum Q shows a similar structure. The dashed red line gives the distribution of vertical MIPs only.

trigger. This increases the purity of the calibration dataset, as the WCD is much more sensitive to muons compared to the EM component of an extensive air shower. For each event that conforms to the selection criteria described above, the maximum pulse height I (peak) and the sum Q (charge) of bins b above a baseline B are calculated as

$$I = \max\left(b - B\right), \qquad Q = \sum_{i=1}^{69} \left(b_i - B\right).$$

We plot the distribution of I and Q in two separate histograms (cf. fig. 3) for 61 s. The filled histograms are sent to internal storage after the integration interval, and the process restarts.

The histograms implement a non-uniform bin size. The bytestream transferred from LS to the CDAS is made up of n_{n} regular bins of size s_{n} that cover the location of I_{MIP} and Q_{MIP}, and n_{s} strided, larger bins of size s_{s} to accommodate more heavily ionizing events. The values of s_{n}, n_{n}, s_{s}, and n_{s} for the peak and charge histogram are

$$\begin{aligned} \text{Peak}: \; & n_{\mathrm{n}} = 100,\; s_{\mathrm{n}} = 2\,\mathrm{ADC}, \qquad n_{\mathrm{s}} = 50,\; s_{\mathrm{s}} = 8\,\mathrm{ADC}; \\ \text{Charge}: \; & n_{\mathrm{s}} = 400,\; s_{\mathrm{s}} = 2\,\mathrm{ADC}, \qquad n_{\mathrm{s}} = 200,\; s_{\mathrm{s}} = 8\,\mathrm{ADC}. \end{aligned}$$

Because the sum Q is by definition higher than the maximum pulse height I, the size of the charge histogram exceeds that of the peak histogram by a factor of four. Entries that exceed the maximum bin value of either histogram are not clipped and are not forwarded to the CDAS.

A typical example of the histograms that the CDAS receives is shown in fig. 3. Both the peak and charge distributions demonstrate similar behavior and have two prominent local maxima. The first maximum at low ADC counts stems from events that satisfy the muon trigger in the WCD but do not raise any signal in the SSD. These are, for example, muons that traverse the water tank but do not hit the scintillator. The second maximum comes from minimally ionizing particles that leave

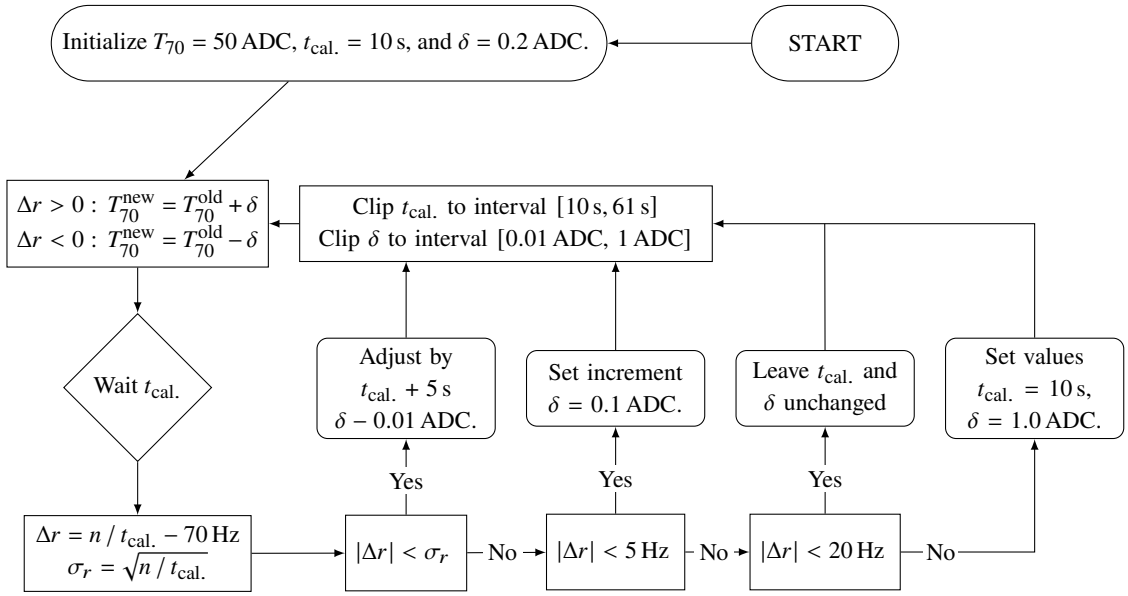

Figure 4: Flowchart describing the rate-based algorithm to approximate I_{MIP} independently on an LS. The idea and implementation details are based on a rate-based calibration of the WCD PMTs as explained in [5].

a characteristic energy deposit in the detector. We estimate the value of I_{MIP} and Q_{MIP} by fitting a second-order polynomial around the region of the second maximum and reading off its vertex and applying the scaling factor from section 3.2. The histogram-based estimate of the MIP peak and charge is referred to as $I_{\text{histo}}^{\text{SSD}}$ and $Q_{\text{histo}}^{\text{SSD}}$, respectively.

This method of calibrating the SSD is very precise. The Poissonian uncertainty on the bin entries is typically $< 3\%$. Using a least-squares optimization algorithm, the resulting statistical uncertainty on the vertex position is of a similar order or smaller. However, this algorithm is used at the CDAS level when the station data are read out during an EAS event reconstruction.

5. Rate based calibration

In the previous section, precise and reliable estimators $I_{\text{histo}}^{\text{SSD}}$ and $Q_{\text{histo}}^{\text{SSD}}$ for the MIP peak and charge are described. However, due to hardware restrictions, it is not feasible to perform the SSD calibration in this way on an SD station. Instead, we opt for a simpler, rate-based algorithm to calibrate the scintillator detector locally. This compromises precision for a finer temporal resolution (O(minute) vs. O(hours)) and can be used to monitor the status of the SSD.

We implement a single-bin threshold trigger with a variable threshold T_{70}, measured in ADC. We count the number of events n in the SSD that satisfy this trigger during an integration window of $t_{\text{cal.}}$. After $t_{\text{cal.}}$ we adjust the threshold by a term δ based on the steps described in fig. 4.

For example, if $n = 730$ trigger events are registered in the first $t_{\text{cal.}} = 10$ s after initialization, we calculate Δr to be 3 Hz. This exceeds $\sigma_r \approx 2.7$ Hz, but not 5 Hz. We therefore set $\delta = 0.1$ ADC,

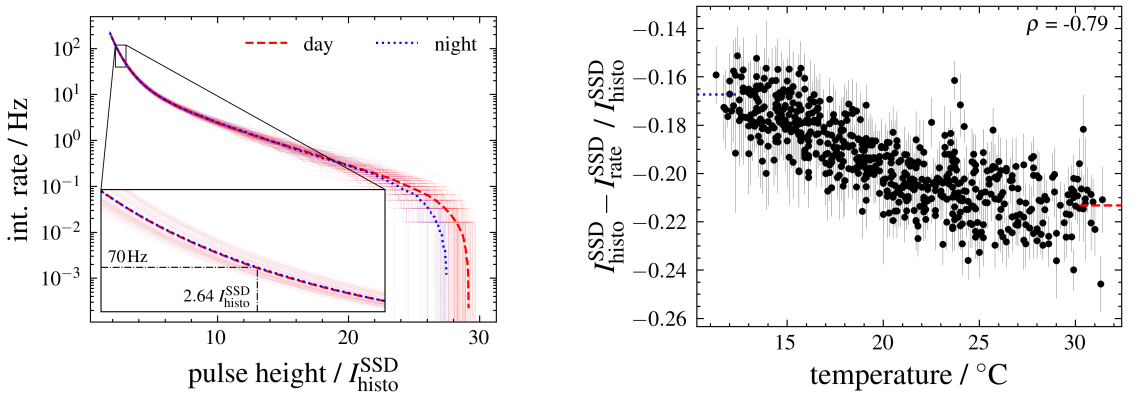

Figure 5: **(a)** The integral rate of events with a peak height of at least I. The rate remains largely unchanged between day and night, and different LS hardware. A 70 Hz trigger rate is observed for a threshold of $T_{70} = 2.64\, I^{SSD}_{histo}$. **(b)** Dependence of the discrepancy between I^{SSD}_{histo} and I^{SSD}_{rate} on ambient temperature. The environmental modulation is not large enough to explain the observed total discrepancy of $\approx 20\%$

and, because $\Delta r > 0$, increase T_{70} by δ. We then collect the number of events that satisfy the updated trigger threshold $T_{70} = 50.1$ ADC for $t_{cal.} = 10$ s, and repeat the above procedure.

In this way, the trigger threshold T_{70} is adjusted until a 70 Hz event rate of the single-bin trigger is reached. Once this is the case, the integration interval $t_{cal.}$ is increased in 5 s-increments to minimize the influence of Poissonian fluctuations on the end result. In doing this, we clip the values $\delta/\text{ADC} \in [0.01, 1.00]$ and $t_{cal.}/\text{s} \in [10, 61]$ respectively. Once the algorithm has reached a full integration interval of 61 s, the current value of T_{70} is saved and the process restarts.

Assuming a constant electronic gain, this algorithm is guaranteed to produce a stable estimate of T_{70}. Next, we establish a relation between T_{70} and I_{MIP}. For this, we collect peak histograms requiring a coincident signal in the WCD, and also measure the spectrum of pulse heights I in the SSD for various SD stations, and different times of day [1]. Using knowledge from coincidence histograms, we express the pulse height spectrum in units of I^{SSD}_{histo}, and calculate the integral rate of events with I above 1 I^{SSD}_{histo}, 2 I^{SSD}_{histo}, et cetera. We compare the results of this analysis for all stations and times of day, and observe no strong dependence on either hardware or temperature differences. The average rate-threshold relationship we obtain this way is visualized in fig. 5a. Specifically, we notice that a 70 Hz rate of the single-bin trigger can be obtained by setting a fixed (in units of I_{MIP}) threshold. We consequently read off the rate-based estimator of I_{MIP} as

$$I^{SSD}_{rate} = T_{70} \,/\, 2.64.$$

The performance of I^{SSD}_{rate} is then evaluated by comparing it with I^{SSD}_{histo}, as done in fig. 6. Evidently, the different estimators are in good agreement only after multiplying a correction factor $C \approx 1.21$ to I^{SSD}_{rate}. The origin of the correction is currently unknown. Differences in hardware among stations have been ruled out as a reason, since C is constant within the expected station-to-station fluctuations of $\approx 5\%$. Furthermore, we note a bias dependent on daytime/temperature in

[1] Once before sunrise (ambient temperature $T \approx 9\,°\text{C}$), and once in the afternoon ($T \approx 27\,°\text{C}$)

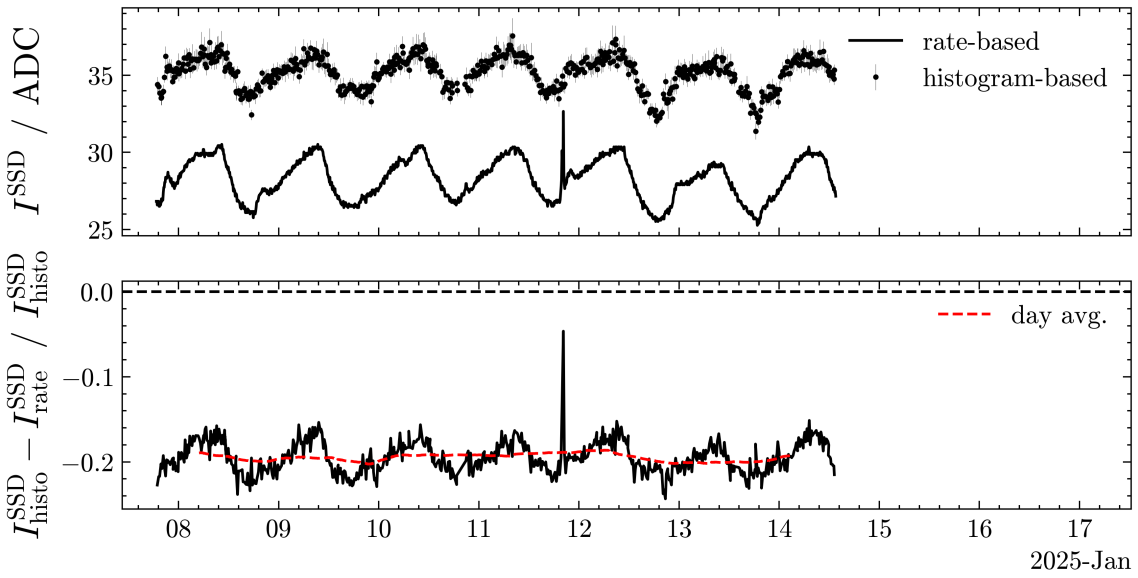

Figure 6: *(top)* I^{SSD}_{histo} and I^{SSD}_{rate} for one LS for an acquisition test spanning roughly one week. *(bottom)* There exists a systematic bias of -20% between I^{SSD}_{histo} and I^{SSD}_{rate}, as well as a daily bias modulation of $\pm 5\%$. The spike in I^{SSD}_{rate} around the 12th of January stems from restarting the data acquisition after hardware problems.

I^{SSD}_{rate}, as displayed in fig. 5b. The effect is, however, not of sufficient amplitude ($\pm 5\%$) to explain the observed discrepancy of $\approx 20\%$. We think the correction factor may be caused by a mistake in the conversion from T_{70} to I^{SSD}_{rate}, and plan to investigate this issue by examining further pulse-height spectra of the SSD.

6. Conclusion

We have explained how to obtain a precise ($\sigma \approx 3\%$) calibration of the SSD by examining the MIP peak and charge distributions. We have proposed an alternative, algorithmically simpler way to calibrate the SSD using a threshold trigger that is optimized to trigger at a fixed rate. We have shown that this rate-based calibration is in good agreement with the histogram-based calibration after a correction factor is applied. The origin of the correction factor currently remains undetermined.

References

[1] R. Sato *et al.*, PoS **ICRC2023**, 373 (2023)

[2] The Pierre Auger Collaboration, Nucl. Instrum. Meth. A **798**, 172-213 (2015)

[3] R. Šmída *et al.*, PoS **ICRC2017**, 390 (2017)

[4] D. Schmidt, KIT, 10.5445/IR/1000093730 (2019)

[5] X. Bertou *et al.*, Nucl. Instrum. Meth. A **568**, 839-846 (2006)

[6] A. Aab *et al.*, arXiv:1604.03637v1 (2016)

[7] P. Assis *et al.*, PoS **ICRC2015**, 620 (2015)